



Au nanoparticles enhanced rutile TiO₂ nanorod bundles with high visible-light photocatalytic performance for NO oxidation

Dieqing Zhang*, Meicheng Wen, Shanshan Zhang, Peijue Liu, Wei Zhu,
Guisheng Li, Hexing Li*

The Education Ministry Key Lab of Resource Chemistry, Shanghai Key Laboratory of Rare Earth Functional Materials, Department of Chemistry, Shanghai Normal University, Shanghai 200234, China

ARTICLE INFO

Article history:

Received 26 July 2013

Received in revised form 6 September 2013

Accepted 22 September 2013

Available online 29 September 2013

Keywords:

NO

Oxidation

Photocatalysis

Rutile

TiO₂

ABSTRACT

A novel Au/TiO₂ visible photocatalyst with Au nanoparticles (NPs) uniformly dispersed onto rutile TiO₂ nanorod bundles was developed and used in photocatalytic NO oxidation for air cleaning. The Au NPs photosensitized TiO₂ in visible-light area *via* plasma effect. They also reduced photoelectron–hole recombination by accelerating electron transfer and promoted NO molecule activation *via* strong adsorption. The TiO₂ acted as a semiconductor photocatalyst and its nanorod bundle structure promoted light harvest by multiple reflections. Moreover, it also acted as a support to highly disperse and stabilize Au nanoparticles. These cooperative promoting effects resulted in the high activity and strong durability of Au/TiO₂ in photocatalytic NO oxidation.

© 2013 Elsevier B.V. All rights reserved.

1. Introduction

The rapid increase of NO_x (NO 90%) released from automobiles and power plants has received great concern due to its danger by forming ground-level ozone, photochemical smog, PM_{2.5}, and adverse effects on the neural system.^[1,2] The thermocatalytic oxidation of NO is frequently employed to remove NO^[3], but they usually have to conduct at very high temperature^[4–6]. It has been reported that Au catalysts with ultrasmall nanoparticle size (<2 nm) display high activity in CO oxidation under low temperature^[7], but they are seldom used in NO oxidation due to the poor activity. Photocatalytic NO oxidation displays advantages in energy-saving, low cost, green and easy operation under mild conditions^[8–11]. More importantly, the strong oxidizing ability of the active sites generated from photocatalysts could oxidize NO into NO₃[−] which could be completely dissolved in water^[8–11], taking into account that the thermocatalytic oxidation of NO mainly produces NO₂ and the adsorption of NO₂ by water will re-release NO. Both theoretical prediction and experimental results indicate that the photocatalytic efficiency mainly depends on the light harvest for generating photocharges and the photoelectron–hole recombination. TiO₂

semiconductor is most frequently employed as photocatalyst owing to its easy availability, cheapness, non-toxicity and stability^[12]. However, it could be activated only by UV light owing to the big energy band gap (3.0–3.2 eV)^[13,14] and also shows poor quantum efficiency due to the photoelectron–hole recombination^[12]. Up to now, a great number of doped TiO₂ have designed to achieve visible photocatalysts^[12,15–18]. Most studies are focused on nonmetal and semiconductor doped TiO₂^[19]. It has also been reported that the TiO₂ doped with metal nanoparticles display spectral response in visible area *via* plasma effect^[20,21], in which the uniform dispersion of metal nanoparticles with ultrasmall size and high stability against gathering play crucial roles in determining the efficiency of plasma effect. Besides, the morphology, porous structure and even the crystal phase also significantly affect the light harvest and photoelectron–hole recombination^[22–26].

Herein, we reported a novel Au/TiO₂ with Au NPs highly dispersed onto rutile TiO₂ nanorod bundles. The Au NPs initiated visible-light-driven photocatalytic NO oxidation *via* plasma effect and also promoted electron transfer to reduce photoelectron–hole recombination as well as activated NO molecules toward oxidation^[20,21]. Besides as a semiconductor photocatalyst, the TiO₂ also acted as a support to deposit and stabilize Au NPs. In addition, the unique TiO₂ nanorod bundle structure promoted light harvest by multiple reflections. These cooperative promoting effects resulted in the high activity of Au/TiO₂ in photocatalytic oxidation of NO under solar and even visible light irradiation.

* Corresponding authors. Tel.: +8621 6432 2272; fax: +8621 6432 2272.

E-mail addresses: dqzhang@shnu.edu.cn (D. Zhang), hexing-li@shnu.edu.cn (H. Li).

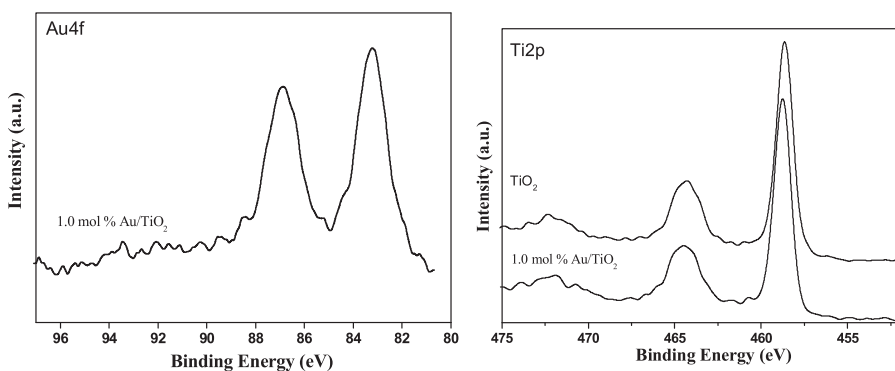


Fig. 1. XPS spectra of pure TiO₂ and 1.0 mol% Au/TiO₂ in Au 4f and Ti 2p levels.

2. Experimental

2.1. Sample preparation

In a typical run of synthesis, 2.0 mL HCl aqueous solution containing 15% TiCl₃ (Merck-Schuchardt) and 8.0 mL deionized H₂O were mixed in a Teflon-lined double-walled digestion vessel, followed by treating at 200 °C for 1 min with a heating rate of 24 °C/min (Ethos TC, Milestone). Then the white precipitate was collected through centrifugation, washed thoroughly with H₂O until pH = 7, and dried in vacuum at 60 °C for 4 h, leading to the rutile TiO₂ nanorod bundles. For comparison, the conventional rutile TiO₂ nanoparticles were also synthesized by microwave heating the mixture of 0.50 mL TiCl₃ and 8.0 mL water at 170 °C for 1 min, followed by treating in the same procedures used for preparing rutile TiO₂ nanorod bundles. Meanwhile, the anatase TiO₂ nanorod bundles were also synthesized by treating a mixture of 2.0 mL HCl aqueous solution containing 15–20% TiCl₃ (Shanghai Qingxi Chemical & Scientific Co.) and 8.0 mL H₂O in a Teflon-lined double-walled digestion vessel at 200 °C for 1 min with a heating rate of 24 °C/min in a microwave, followed by washing and drying procedure as described above. All the Au/TiO₂ samples were prepared by 20 min UV light irradiating a mixture containing 0.13 g TiO₂, 31 mL H₂O, 2.0 mL CH₃OH, and desired amount of HAuCl₄·4H₂O under mild stirring. The precipitate was collected through centrifugation, followed by washing and drying in the procedures described above. The HAuCl₄ concentration was adjusted for achieving desired Au loadings.

2.2. Characterization

The crystal phase was determined by X-ray diffraction (XRD, Bruker D8 Cu-K α). The N₂ adsorption–desorption isotherms were recorded at 77 K using a Micromeritics AsAP 2010 instrument. The specific surface area (S_{BET}), pore volume (V_p) and pore diameter (D_p) were calculated by applying Brunauer–Emmett–Teller (BET) and Barrett–Joyner–Halenda (BJH) models on desorption branches. Particle size and morphologies were observed on a transmission electron microscopy (TEM, JEOL-2010F, 200 kV) and a field scanning electron microscopy (FESEM, FEI Quanta 400 FEG). The UV–Vis diffuse reflectance spectra (DRS) were obtained on a Varian Cary 100 Scan UV–Vis system. The photoluminescent spectra (PLS) were examined on a Varian Cary-Eclipse 500. Surface electronic states were analyzed on an X-ray photoelectron spectroscopy (XPS, PHI Quantum 2000 Al-K α). All the binding energy values were calibrated by using C_{1s} = 284.8 eV as a reference. Electron spin resonance (ESR) spectra were obtained using a Bruker model ESP 300E ESR spectrometer.

2.3. Photoelectrochemical measurement

Photoelectrochemical measurements were carried out in a conventional three-electrode, single-compartment quartz cell on an electrochemical station (CHI 660D). The Au/TiO₂ electrodes with an active area of ca. 4.0 cm² were served as working electrode. The counter electrode and the reference electrode were platinum sheet and saturated calomel electrode (SCE), respectively. A bias voltage of 0.50 V was utilized for driven the photo-generated electrons transfer from working electrode to platinum electrode. A 300 W tungsten halogen lamp located at 10 cm away from the photoelectrochemical cell was used as a source of simulated solar light and the visible light ($\lambda > 400$ nm) obtained by cutting the light with wavelength shorter than 400 using an ultraviolet filter. A 0.20 M Na₂SO₄ aqueous solution was used as the electrolyte.

2.4. Activity test

The photocatalytic NO oxidation in gas phase was carried out at ambient temperature in a continuous flow reactor with volume of 4.5 L (10 × 30 × 15 cm). During solar light driven photocatalysis, a 300 W tungsten halogen lamp (General Electric) located vertically above the reactor was used as the simulated sunlight. For the visible light driven photocatalysis, a piece of Pyrex glass was employed to cut off all the UV light with the wavelength below 400 nm. Four minifans were fixed around the lamps to cool the system. In each run of experiments, an air gas flow containing 400 ppb NO (humidity level of 70%) was allowed to pass through 0.10 g photocatalyst at the rate of 4.0 L/min. After reaching adsorption–desorption equilibrium on the photocatalyst, the lamp was turned on to start the photocatalysis reaction. The blank experiments demonstrated that no significant NO oxidation occurred in the absence of either light irradiation or photocatalyst. The photocatalysts were washed with D.I. water before each run of recycling test. The NO₂ product was qualitatively identified by a gas chromatograph (GC) and the NO₃[−] was detected by using an ion chromatograph (IC). The concentration of NO was continuously measured by using a chemiluminescence NO analyzer (Thermo Environmental Instruments Inc. Model 42c). The NO removal rate (%) was calculated based on the following equation: NO removal rate (%) = (C₀ − C)/C₀ × 100%, where C₀ and C refer to the NO concentration determined before and after reaction.

3. Results and discussion

3.1. Photocatalysts characterization

The rutile TiO₂ in nanorod bundles was synthesized by microwave-assisted hydrothermal treatment of TiCl₃, followed by

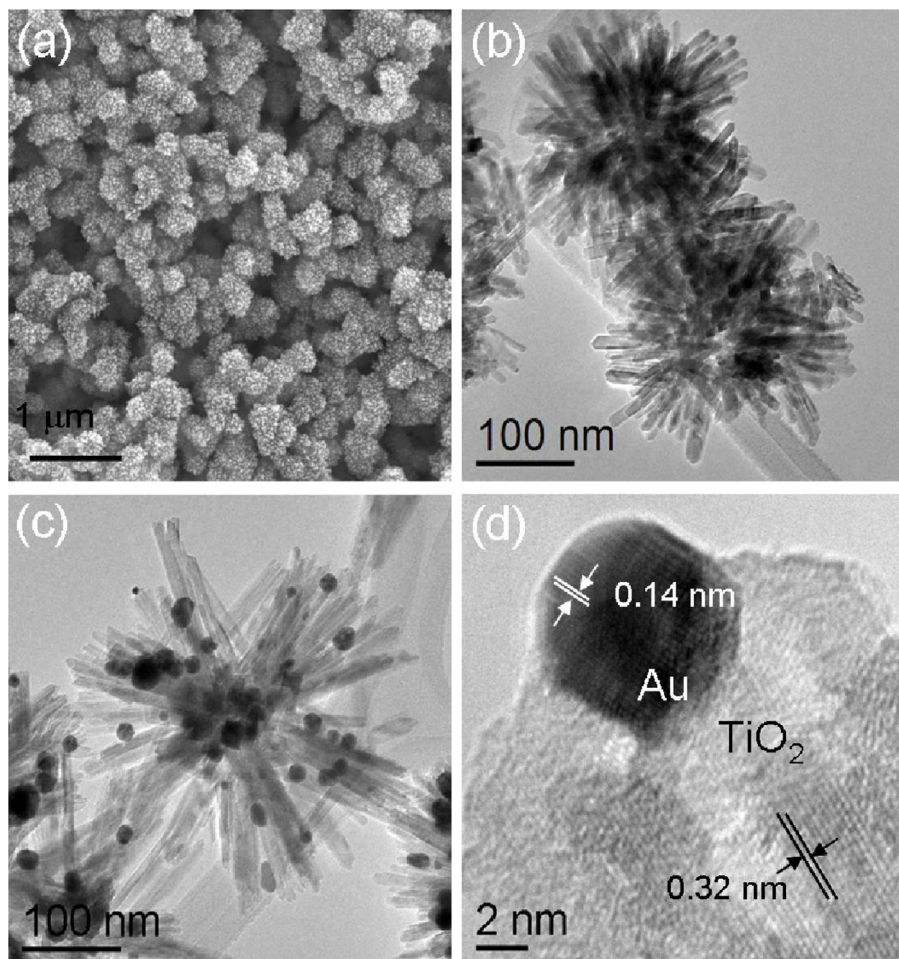


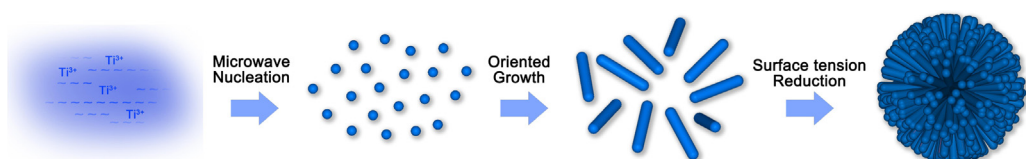
Fig. 2. FESEM (a) and TEM (b) images of rutile TiO_2 , together with TEM (c) and HRTEM (d) images of 1.0 mol% Au/ TiO_2 .

anchoring Au NPs through *in-situ* reduction of HAuCl_4 in aqueous solution containing the as-received TiO_2 . The XPS spectra (Fig. 1) revealed that all the Au species in 1.0 mol% Au/ TiO_2 were present in metallic state, corresponding to the binding energy (BE) around 83.3 eV in $\text{Au}_{4f7/2}$ level. In comparison with the standard BE of pure Au metal, the Au in Au/ TiO_2 displayed a negative BE shift by 0.7 eV. Meanwhile, the BE of Ti^{4+} in Au/ TiO_2 shifted positively by 0.2 eV comparing to that observed in pure rutile TiO_2 . These results confirmed the strong interaction between Au and rutile TiO_2 , leading to partial electron transfer from TiO_2 to Au via d-p feedback bond [22].

As shown in Fig. 2a and b, both FESEM and TEM images revealed that the pure TiO_2 was present in spherical morphology. It composed of nanorods with average length and width around 150 nm and 10 nm, respectively. Taking into account that the Gibbs energy of rutile TiO_2 increased in the order of (110), (100), (101), and (001) facets [27,28], the TiO_2 nanorods were formed due to the oriented crystal growth along the [001] direction (see Scheme 1). The aspect ratio was estimated as 15 by dividing the length of the major

axis with the width of the minor axis. These TiO_2 nanorods gathered into uniform spherical bundles to reach thermodynamically stable state. The TEM image of 1.0 mol% Au/ TiO_2 (Fig. 2c) demonstrated that, after *in situ* reduction of HAuCl_4 under UV light irradiation, ultrasmall Au nanoparticles with average diameter around 8.5 nm were uniformly dispersed onto the surface of TiO_2 nanorod bundles. Meanwhile, the HRTEM image (Fig. 2d) clearly displayed periodic fringe spaces of 0.32 nm and 0.14 nm indicative of highly crystallized rutile TiO_2 and face-centered-cubic (fcc) Au metal, together with the formation of heterojunctions at the interface between Au and TiO_2 .

Both pure rutile TiO_2 and 1.0 mol% Au/ TiO_2 displayed typical type-IV N_2 adsorption-desorption isotherm (Fig. S1) indicative of mesoporous structure. As shown in Table 1, the pure TiO_2 and the Au/ TiO_2 with different Au loadings exhibited similar specific surface area (S_{BET}), pore volume (V_p) and pore diameter (D_p), implying that the Au NPs were mainly deposited onto outer surface of TiO_2 nanorod bundles rather than filled into mesoporous channels. After being crushed, the original nanorod bundles

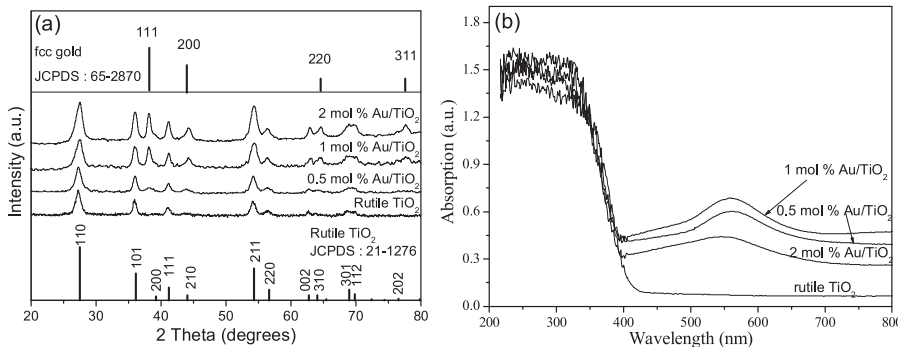


Scheme 1. Illustration of the formation of TiO_2 nanorod bundles.

Table 1

Structural parameters and activities of different photocatalysts in photocatalytic NO oxidation.

Photocatalyst	D_{Au} (nm)	S_{BET} (m^2/g)	V_p (cm^3/g)	D_p (nm)	Max. NO conversion (%)	
					Solar light	Visible light
TiO ₂	/	105	0.12	9.9	19	9.0
0.50 mol% Au/TiO ₂	5.6	101	0.11	9.8	38	23
1.0 mol% Au/TiO ₂	8.5	96	0.11	9.8	50	31
2.0 mol% Au/TiO ₂	33	87	0.10	9.6	33	19
Crushed 1.0 mol% Au/TiO ₂	8.5	99	0.11	9.8	/	24
Conventional 1.0 mol% Au/TiO ₂	8.6	58	0.090	11	/	20
1.0 mol% Au/TiO ₂ reused for 3 times	8.5	95	0.11	9.8	/	29

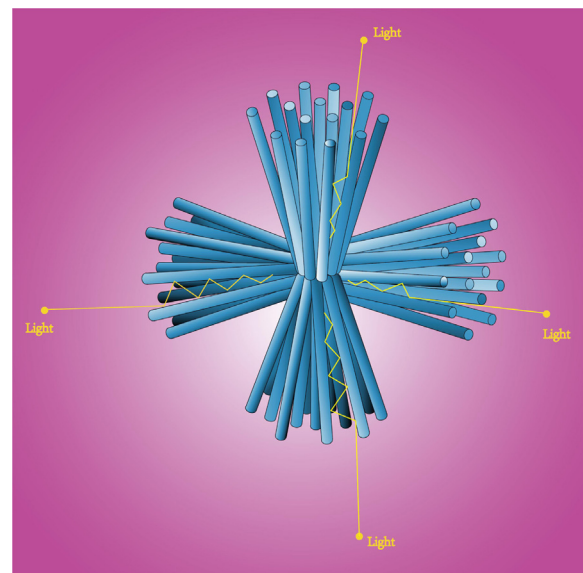
Reaction conditions: a 4.5 L reactor, 0.10 g photocatalyst, air flow containing 400 ppb NO and 70% humidity at speed of 4.0 L/min, 300 W solar light or visible light ($\lambda \geq 400 \text{ nm}$).**Fig. 3.** XRD patterns (a) and diffuse reflectance UV-Vis spectra (b) of pure rutile TiO₂ and Au/TiO₂ with different Au loadings.

were damaged into nanoparticles (see the FESEM image in Fig. S2a), but S_{BET} , V_p and D_p values remained unchanged, suggesting the preservation of mesoporous structure. Although the conventional 1.0 mol% Au/TiO₂ in nanoparticles displayed similar N₂ adsorption–desorption isotherm, V_p and D_p to the 1.0 mol% Au/TiO₂ in nanorod bundles, it exhibited much lower S_{BET} , obviously due to big particle size (see the FESEM image in Fig. S2b).

The XRD patterns in Fig. 3a revealed that the pure TiO₂ was present in typical rutile phase, corresponding to (110), (101), (200), (111), (210), (211), (220), (002), (310), (301), (112) and (202) diffraction signals around 2θ of 27.4°, 36.1°, 39.2°, 41.3°, 44.1°, 54.3°, 56.6°, 62.8°, 64.1°, 69.0°, 70.0°, 76.6° (JCPDS: 21-1276). The presence of Au NPs had no significant influence on the crystal phase of rutile TiO₂. The metal Au in face-centered-cubic (fcc) nanocrystal could also be clearly identified from (111), (200), (220) and (311) diffractions around 2θ of 38.2°, 44.4°, 64.6° and 77.6° (JCPDS: 65-2870). Based on the calculation from Scherrer equation, the Au crystallite size was estimated as 5.6°, 8.5° and 33 nm in Au/TiO₂ with Au loading of 0.50°, 1.0° and 2.0 mol% (see Table 1).

The UV–Vis spectra (Fig. 3b) revealed that rutile TiO₂ displayed only very little light absorbance for visible light with wavelength (λ) closed to 400 nm, which was consistent with the light absorbance calculated from the energy band gap of rutile (3.0 eV). The Au/TiO₂ displayed spectral response in visible light area centered at 550 nm, obviously owing to the plasma effect from Au NPs [29]. With the increase of Au loading from 0.50 mol% to 1.0 mol%, the absorbance for visible light enhanced owing to the increased number of Au NPs. However, further increase of Au loading to 2.0 mol% caused an abrupt decrease in visible light absorbance, which could be attributed to the gathering of Au NPs into big nanoparticles (33 nm), taking into account that the plasma effect occurred only at very tiny Au nanoparticles with size smaller than 10 nm [30]. The 1.0 mol% Au/TiO₂ in nanorod bundles exhibited much stronger light absorbance in visible region than either the crushed 1.0 mol% Au/TiO₂ or the conventional 1.0 mol% Au/TiO₂ in nanoparticles (Fig. S3). This could possibly be attributed to the

enhanced light harvest via multiple reflections (see the model in Fig. 4). The 1.0 mol% Au/TiO₂ exhibited stronger photocurrent than either the 2.0 mol% or the 0.50 mol% Au/TiO₂ under visible light irradiation (Fig. 5a) owing to the enhanced plasma effect by Au NPs. It also displayed stronger photocurrent than either the 2.0 mol% or the 0.50 mol% Au/TiO₂ under UV light ($\lambda = 365 \text{ nm}$) irradiation (Fig. 5b), which could be mainly attributed to the lower recombination rate between photoelectrons and holes, taking into account that these three Au/TiO₂ samples displayed similar absorbance for UV light at 365 nm (see Fig. 3b). The photoluminescence (PL) emission spectra (Fig. S4) clearly demonstrated that the 1.0 mol% Au/TiO₂ displayed much lower intensity of the

**Fig. 4.** Schematic illustration of multiple light reflections within Au/TiO₂ nanorod bundles.

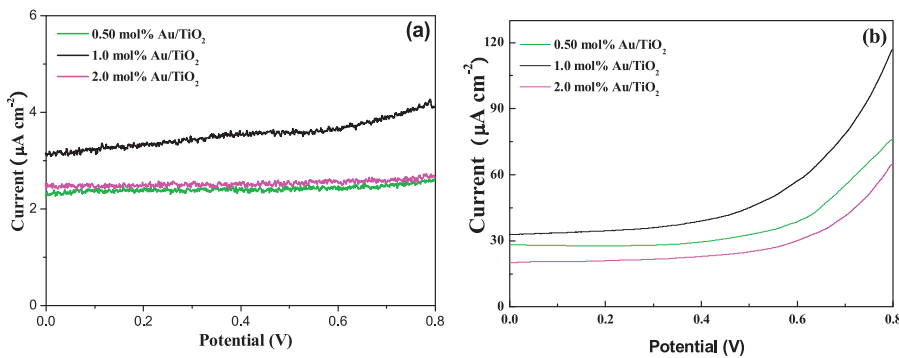


Fig. 5. Photocurrent tests of Au/TiO₂ with different Au loadings irradiated by (a) visible light ($\lambda > 400 \text{ nm}$) and (b) UV light ($\lambda = 365 \text{ nm}$).

peak around 560 nm than pure TiO₂ and other Au/TiO₂ samples, corresponding to lower photoelectron-hole recombination rate [31]. Obviously, the metallic Au promoted electron transfer, which facilitated separation of photoelectrons from holes.

3.2. Photocatalytic activity

The gas-phase photocatalytic NO oxidation was performed under irradiation of either solar light or visible light (see the experimental setup in Fig. S5). Our preliminary tests demonstrated that no significant decrease in NO content was observed in the absence of either light irradiation or photocatalyst, suggesting that the NO oxidation was mainly driven by photocatalysis. The main product was determined as NO₃⁻ by IC analysis, and only little NO₂ was detected by GC analysis. Based on the reaction profiles (Fig. 6) and the maximum NO conversions (Table 1), we may obtain the following results: (1) The pure rutile TiO₂ exhibited low activity under visible-light irradiation ($\lambda \geq 400 \text{ nm}$) since it could be activated

only by visible light with λ closed to 400 nm due to the big energy bad gap (3.0 eV). This could be confirmed by the fact that the pure anatase TiO₂ displayed no significant activity under visible light irradiation since the anatase could be activated only by UV light with $\lambda \leq 386 \text{ nm}$ due to the enhanced energy band gap (3.2 eV). (2) The rutile TiO₂ exhibited enhanced activity under solar light irradiation owing to the presence of 2–5% UV light. Similar results were also obtained by using other photocatalysts. (3) The Au/TiO₂ exhibited much higher activity than the pure TiO₂ under both solar light and visible light irradiations. An important reason was the plasma effect from the Au quantum dots. As shown in Scheme 2, photoelectrons generated from Au quantum dots under visible light, which transferred onto conduction band of TiO₂ semiconductor [32,33], followed by reducing O₂ to form ·O₂⁻ active sites for NO oxidation. Meanwhile, such plasma effect also induced excitation of electrons on valence band of TiO₂ semiconductor owing to the presence of Au^{δ+}, leading to formation of holes which subsequently oxidized H₂O into ·OH active sites for NO oxidation. Besides, the

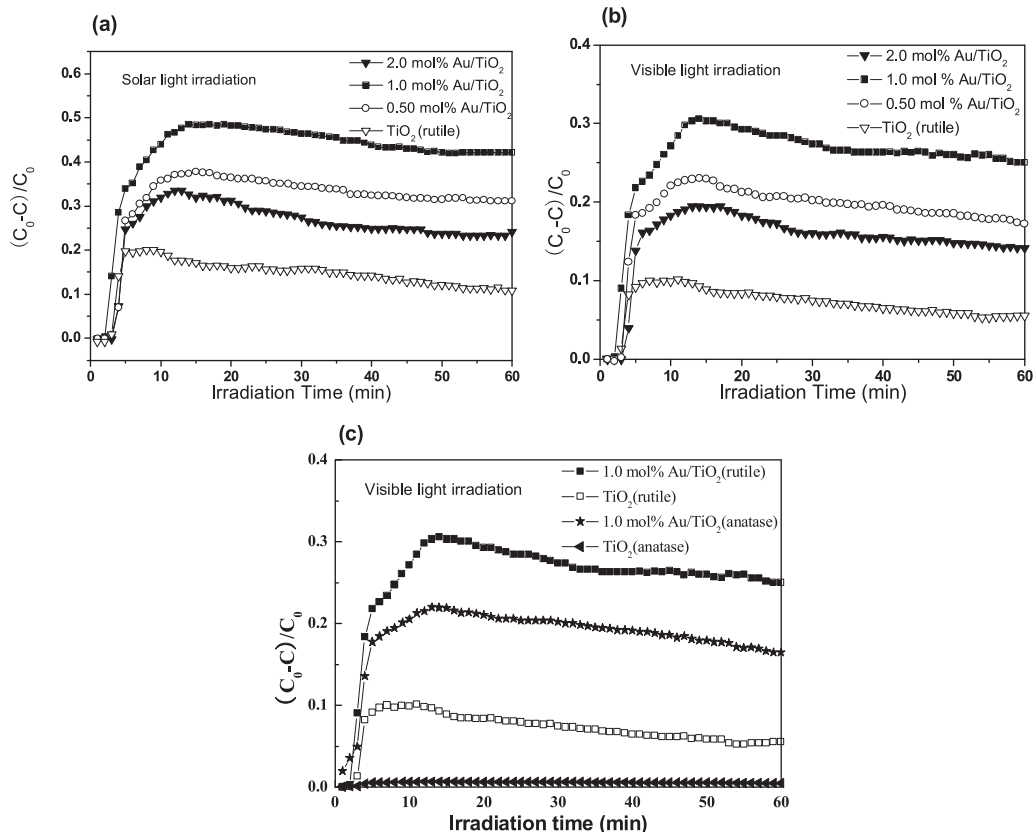
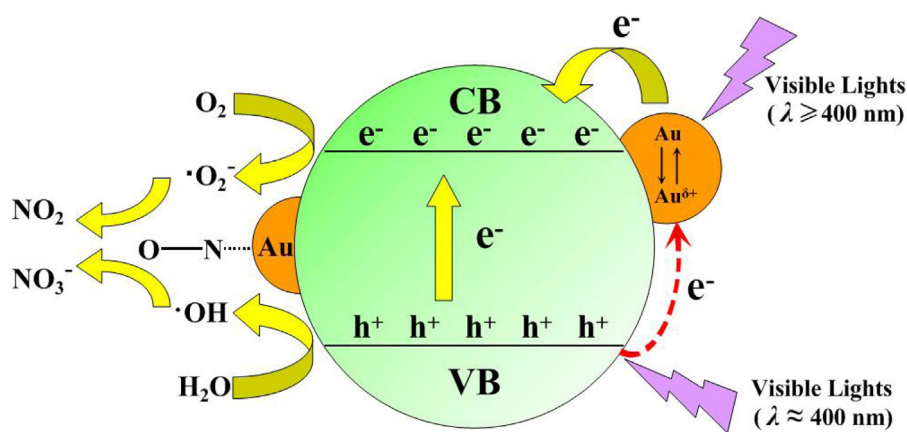


Fig. 6. Reaction profiles of photocatalytic NO oxidation in a single pass flow. Reaction conditions are given in Table 1.



Scheme 2. A plausible mechanism for visible light induced photocatalytic NO oxidation on Au/TiO₂.

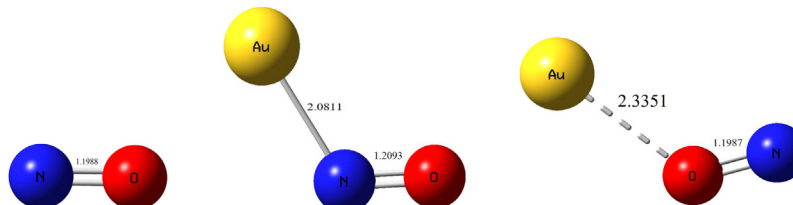


Fig. 7. Adsorption models of NO molecule on the Au nanoparticle.

Au also served as an electric conductor to promote the electron transfer, which facilitated the separation of photoelectrons from holes, leading to the decreased photoelectron–hole recombination rate. Furthermore, the Au also activated NO molecule via strong adsorption. Considering two adsorption models (Fig. 7), the density functional theory (DFT) calculation revealed that the N–O bond length did not change in the Au···O–N adsorption model, implying that no chemical bond was formed. However, the N–O bond length increased from 0.11988 nm to 0.12093 nm in the Au···O–N adsorption model, showing the formation of Au–N chemical bond, leading to the decreased N–O bond strength. According to the frontier orbital theory, the HOMO energy of the NO molecule increased while the LUMO energy decreased after NO being adsorbed on Au (see Table 2). Based on the proposed molecular orbital diagram (Fig. 8), the high energy of HOMO favored NO oxidation since the electrons could be easily removed [34–36]. With the increase of Au loading from 0.50 mol% to 1.0 mol%, the activity of Au/TiO₂ increased owing to the increased number of Au quantum dots. However, further increase of Au loading from 1.0 mol% to 2.0 mol% resulted in an abrupt decrease in activity due to the gathering of Au quantum dots into big particles. (4) Although the 1.0 mol% Au/TiO₂ (rutile) displayed similar absorbance for visible light to the 1.0 mol% Au/TiO₂ (anatase) owing to the similar nanorod bundle structure for light harvesting and Au particle size for plasma effect (see Fig. S6), it still exhibited much higher activity under irradiation with visible light at $\lambda \geq 400$ nm, which could mainly be attributed the higher activity of rutile TiO₂ than that of anatase TiO₂. (5) It was also found that the 1.0 mol% Au/TiO₂ exhibited higher activity than either the crushed 1.0 mol% Au/TiO₂

or the conventional 1.0 mol% Au/TiO₂ in nanoparticles, which could be attributed to the enhanced light harvest via multiple reflections (see Fig. 4). Meanwhile, the large aspect ratio of rutile nanorods also contributed to the fast electron transfer because the precisely oriented nature of the nanorod architecture made them excellent electron percolation pathways for vectorial charge transfer, thereby reducing photoelectron–hole recombination rate [37].

Fig. S7a demonstrated that the 1.0 mol% Au/TiO₂ could be used repetitively for three times without significant decrease in activity in photocatalytic NO oxidation under visible light irradiation, showing excellent durability of the Au/TiO₂ photocatalyst, which could also account for the long period steady state during photocatalytic NO oxidation (see Fig. 6). The ICP analysis confirmed

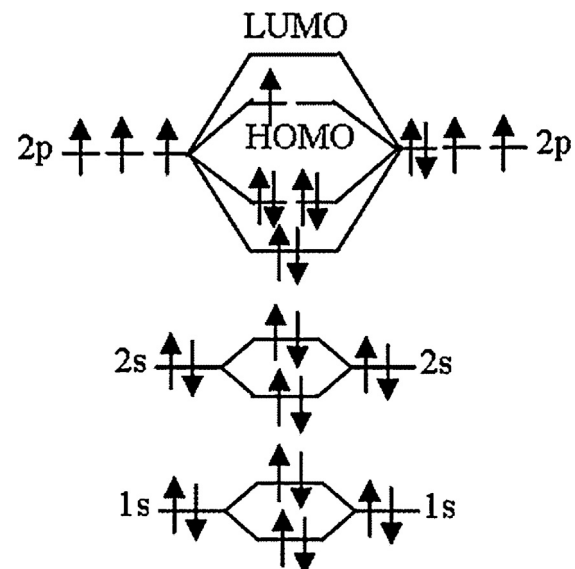


Fig. 8. Molecular orbital diagram of NO molecule.

Table 2

The energy of HOMO and LUMO of the NO molecule before and after being adsorbed on metallic Au.

Molecule	HOMO (eV)	LUMO (eV)
N–O	-6.6878	-3.7530
Au···O–N	-6.6372	-4.2014

the absence of Au leaching during photocatalysis. Meanwhile, as shown in Fig. S7b, the TEM image demonstrated that no significant agglomeration of Au quantum dots occurred in the Au/TiO₂ photocatalyst after being reused for three times. Obviously, the strong interaction between Au quantum dots and the TiO₂ support played a key role in stabilizing Au quantum dots against leaching and gathering. Furthermore, it was also found that the nanorod bundle structure of the Au/TiO₂ photocatalyst was well preserved after being reused for three times, showing the strong hydrothermal stability.

4. Conclusions

In summary, this work developed a novel Au/TiO₂ with Au quantum dots uniformly dispersed onto rutile TiO₂ nanorod bundles. This Au/TiO₂ exhibited high activity and strong durability in visible light induced photocatalytic NO oxidation owing to cooperative promoting effects from both the Au quantum dots and the TiO₂ nanorod bundles in generating photosensitization, activating NO molecules, reducing photoelectron–hole recombination, enhancing light harvest, and stabilizing Au quantum dots. It supplied a platform to design ultrasmall Au nanoparticles with strong stability against either leaching or gathering, which may offer more opportunities for Au catalyst applications.

Acknowledgments

This work was supported by NSFC 21007040, 21207090, 21261140333, 21237003, 12PJ1406800, 11PJ1407500, 11ZR1426300, 12YZ079, IRT1269, the Doctoral program of Higher Education (20123127120009) and the scheme administrated by Shanghai Normal University (DXL122).

Appendix A. Supplementary data

Supplementary data associated with this article can be found, in the online version, at <http://dx.doi.org/10.1016/j.apcatb.2013.09.042>.

References

[1] A. Fritz, V. Pitchon, *Appl. Catal., B: Environ.* 13 (1997) 1–25.

- [2] H. Bosch, F. Janssen, *Catal. Today* 2 (1988) 369–531.
- [3] X.L. Tang, J.M. Hao, W.G. Xu, J.H. Li, *Catal. Commun.* 8 (2007) 329–334.
- [4] T. Mysdéra, *Appl. Catal., B: Environ.* 2 (1993) 199–205.
- [5] X. Shuilm, *J. Catal.* 188 (1999) 24–31.
- [6] G. Busca, L. Lietti, G. Ramis, F. Bertì, *Appl. Catal., B: Environ.* 18 (1998) 1–36.
- [7] C.Y. Liu, Y.Z. Tian, S.S. Lin, H. Li, X.J. Wu, L. Li, Y. Pei, X.C. Zeng, *J. Am. Chem. Soc.* 135 (2013) 2583–2595.
- [8] G.S. Li, D.Q. Zhang, J.C. Yu, *Environ. Sci. Technol.* 43 (2009) 7079–7085.
- [9] G.S. Li, D.Q. Zhang, J.C. Yu, *Chem. Mater.* 20 (2008) 3983–3992.
- [10] S.X. Ge, L.Z. Zhang, *Environ. Sci. Technol.* 45 (2011) 3027–3033.
- [11] I. Nakamura, N. Negishi, S. Kutsuna, T. Ihara, S. Sugihara, K. Takeuchi, *J. Mol. Catal., A: Chem.* 161 (2000) 205–212.
- [12] M.R. Hoffmann, S.T. Martin, W. Choi, D.W. Bahnemann, *Chem. Rev.* 95 (2002) 69–96.
- [13] J. Zhang, Y. Wu, M. Xing, S.A.K. Leghari, S. Sajjad, *Energy Environ. Sci.* 3 (2010) 715–726.
- [14] Y. Cong, J.L. Zhang, F. Chen, M. Anpo, *J. Phys. Chem. C* 111 (2007) 6976–6982.
- [15] M.S. Chen, W. Goodman, *Science* 306 (2004) 252–255.
- [16] P.X. Huang, F. Wu, B.L. Zhu, X.P. Gao, H.Y. Zhu, T.Y. Yan, W.P. Huang, S.H. Wu, D.Y. Song, *J. Phys. Chem. B* 109 (2005) 19169–19174.
- [17] E. Formo, Z. Peng, E. Lee, X. Lu, H. Yang, Y. Xia, *J. Phys. Chem. C* 112 (2008) 9970–9975.
- [18] Y. Lee, M.A. Garcia, N.A.F. Huls, S. Sun, *Angew. Chem. Int. Ed.* 49 (2010) 1271–1274.
- [19] D.Q. Zhang, G.S. Li, H.X. Li, Y.F. Lu, *Chem. Asian J.* 8 (2013) 26–40.
- [20] D.B. Ingram, S. Linic, *J. Am. Chem. Soc.* 133 (2011) 5202–5205.
- [21] W.J. Li, D.Z. Li, J.J. Xian, W. Chen, Y. Hu, Y. Shao, X.Z. Fu, *J. Phys. Chem. C* 114 (2010) 21482–21492.
- [22] H.X. Li, Z.F. Bian, J. Zhu, D.Q. Zhang, G.S. Li, Y.N. Huo, H. Li, Y.F. Lu, *J. Am. Chem. Soc.* 129 (2007) 8406–8407.
- [23] H.X. Li, Z.F. Bian, J. Zhu, Y.N. Huo, H. Li, Y.F. Lu, *J. Am. Chem. Soc.* 129 (2007) 4538–4539.
- [24] Y.B. Zhao, W.H. Ma, Y. Li, H.W. Ji, C.C. Chen, H.Y. Zhu, J.C. Zhao, *Angew. Chem. Int. Ed.* 51 (2012) 3188–3192.
- [25] D.Q. Zhang, G.S. Li, J.C. Yu, *Chem. Commun.* (2009) 4381–4383.
- [26] J. Zhu, S.H. Wang, Z.F. Bian, S.H. Xie, C.L. Cai, J.G. Wang, H.G. Yang, H.X. Li, *CrystEngComm* 12 (2010) 2219–2224.
- [27] A. Tsujiko, T. Kisumi, Y. Magari, K. Murakoshi, Y. Nakato, *J. Phys. Chem. B* 104 (2000) 4873–4879.
- [28] B.J. Morgan, G.W. Watson, *J. Phys. Chem. C* 113 (2009) 7322–7328.
- [29] M. Alvaro, B. Cojocaru, A.A. Ismail, N. Petrea, B. Ferrer, F.A. Harraz, V.I. Parvulescu, H. Garcia, *Appl. Catal., B: Environ.* 99 (2010) 191–197.
- [30] S. Link, M.A. El-Sayed, *J. Phys. Chem. B* 103 (1999) 8410–8426.
- [31] H.X. Li, G.S. Li, J. Zhu, Y. Wan, *J. Mol. Catal. A: Chem.* 226 (2005) 93–99.
- [32] Z.W. Seh, S.H. Liu, M. Low, S.Y. Zhang, Z.L. Liu, A. Mlayah, M.Y. Han, *Adv. Mater.* 24 (2012) 2310–2314.
- [33] D. Tsukamoto, Y. Shiraishi, Y. Sugano, S. Ichikawa, S. Tanaka, T. Hirai, *J. Am. Chem. Soc.* 134 (2012) 6309–6315.
- [34] H.Y. Kim, H.M. Lee, G. Henkelman, *J. Am. Chem. Soc.* 134 (2012) 1560–1570.
- [35] I.X.Y. Green, W.J. Tang, M. Neurock, J.T. Yates Jr., *Science* 333 (2011) 736–739.
- [36] M. Valden, X. Lai, D. Goodman, *Science* 281 (1998) 1647–1650.
- [37] G.S. Li, L. Wu, F. Li, P.P. Xu, D.Q. Zhang, H.X. Li, *Nanoscale* 5 (2013) 2118–2125.